NASA Technical Paper 3016

September 1990

Thermal-Distortion Analysis of an Antenna Strongback for Geostationary High-Frequency Microwave Applications

Jeffery T. Farmer,
Deborah M. Wahls,
and Robert L. Wright

NASA

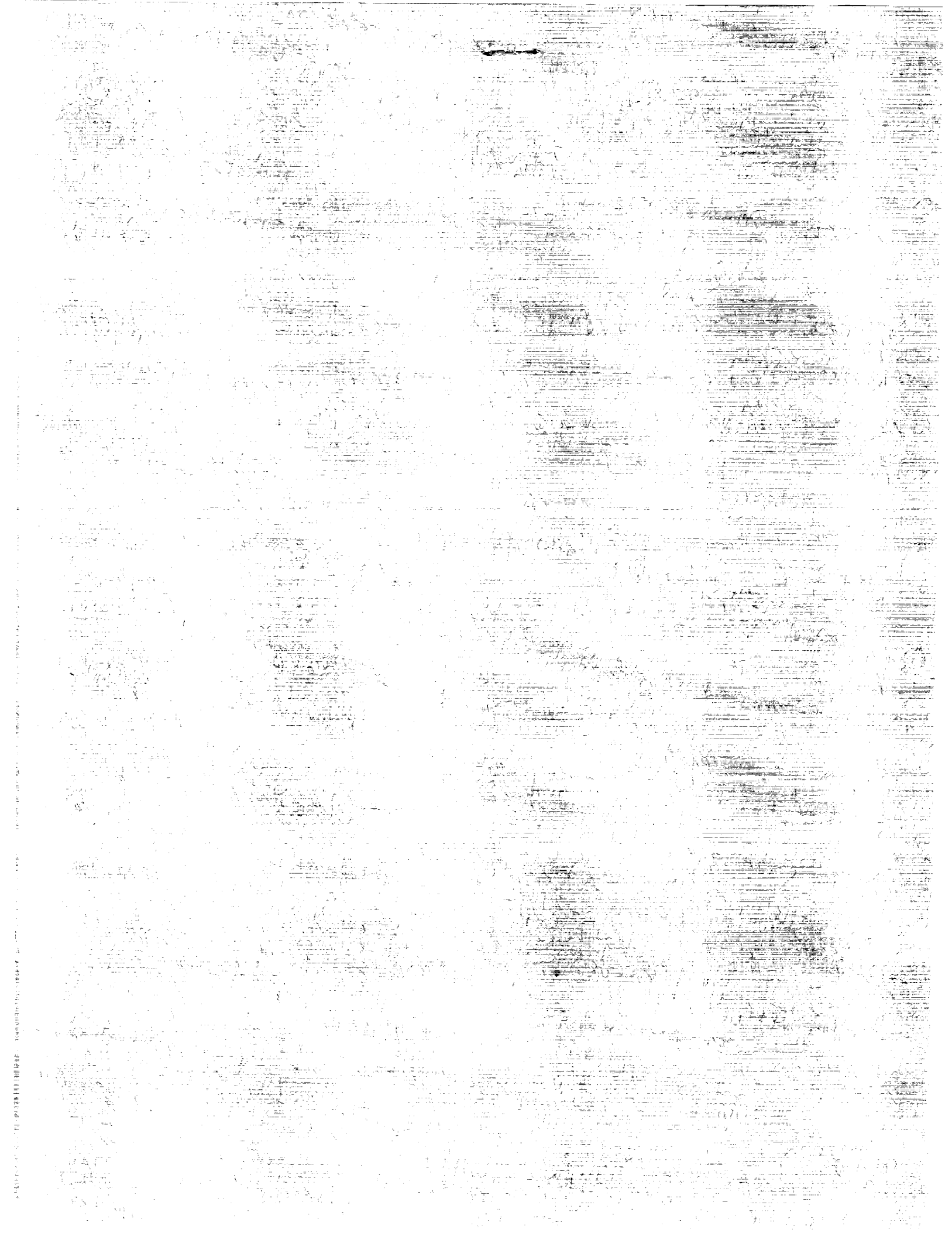

NASA Technical Paper 3016

1990

Thermal-Distortion Analysis of an Antenna Strongback for Geostationary High-Frequency Microwave Applications

Jeffery T. Farmer,
Deborah M. Wahls,
and Robert L. Wright
Langley Research Center
Hampton, Virginia

National Aeronautics and Space Administration
Office of Management
Scientific and Technical Information Division

Summary

The Global Change Technology Initiative calls for a geostationary platform for Earth-science monitoring. One of the major science instruments is the high-frequency microwave sounder (HFMS) which uses a large-diameter, high-resolution, high-frequency microwave antenna. The size and required accuracy of this antenna dictate the need for a segmented reflector, and on-orbit disturbances may be a significant factor in its design. A study was performed to examine the effects of the geosynchronous thermal environment on the performance of the strongback structure for a proposed antenna concept for this application. The study included definition of the strongback and a corresponding numerical model to be used in the thermal and structural analyses, definition of the thermal environment, determination of structural element temperatures throughout potential orbits, estimation of resulting thermal distortions, and assessment of the capability of the structure to meet surface accuracy requirements. Analyses show that shadows produced by the antenna reflector surface play a major role in increasing thermal distortions. Through customization of surface coatings and element expansion characteristics, the segmented reflector concept can meet the strict surface accuracy requirements.

Introduction

NASA is proposing a Global Change Technology Initiative (GCTI) program. Its purpose will be to develop the spacecraft, data systems, and instruments required to measure global biogeochemical, atmospheric, and oceanographic changes in the Earth's environment from space. A combination of low Earth orbit (LEO) and geosynchronous Earth orbit (GEO) multiinstrument spacecraft or large platforms will provide scientific data to help scientists better characterize the current environmental conditions and understand surface, atmospheric, and oceanographic energy and chemical transport mechanisms. A comprehensive set of science issues and associated instruments that would take advantage of the long dwell times and the hemispherical coverage available at geostationary orbit have been compiled in reference 1. A geostationary Earth-science platform that could support these instruments has been developed and is shown in figure 1. This spacecraft concept supports over 15 different instruments with widely diverse requirements. It is designed to provide a stable, stiff platform for pointing accuracy. Although most of the instruments are relatively small in size, the high- and low-frequency microwave radiometers require large-diameter antennas with extremely accurate surface contours.

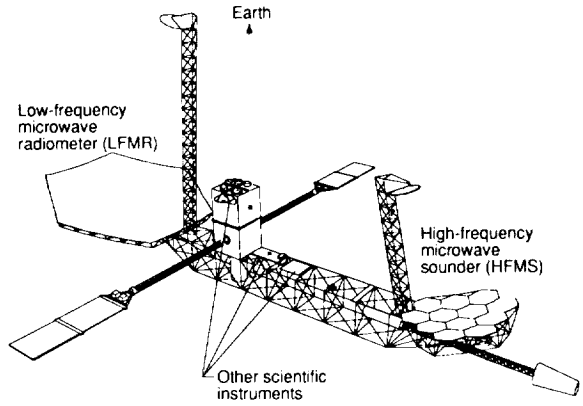

Figure 1. Geostationary Earth-science platform.

In this study, an antenna structure concept capable of meeting the accuracy requirements as well as packageability constraints imposed by available transportation systems has been developed from existing structural technology for the high-frequency radiometer. Since the achievable surface accuracy depends on the magnitude of thermal distortions experienced by the supporting structure, a thermal analysis and assessment of the resulting surface distortions was conducted and is presented for two typical geosynchronous orbits. The effects of utilizing advanced low-thermal-expansion materials and thermal coatings are also discussed.

Geostationary Platform Description

Spacecraft

The conceptual design of the spacecraft for the geostationary Earth-science missions is shown in figure 1 and described in reference 1. The spacecraft incorporates a box truss concept (based on the Space Station Freedom structural design) to provide the required stiffness to the platform. Science instruments and power, pointing, and communications packages are mounted along the platform. The configuration is dominated by the low-frequency microwave radiometer (LFMR) and the high-frequency microwave sounder (HFMS) antennas. The LFMR is a large-aperture antenna operating at frequencies ranging from 6 to 37 GHz. In this range, a mesh or membrane reflector surface may provide adequate performance. The HFMS, on the other hand, operates between 60 and 220 GHz which necessitates the use of a high-accuracy, solid-reflector surface. This high accuracy is very susceptible to thermal distortion of the supporting structure (strongback). The opacity of the surface further aggravates the distortion problem by causing significant temperature variations in

the supporting structure. The analysis in this paper examines the thermal distortion characteristics of possible structural design concepts for this antenna. A structural dynamics analysis of the complete spacecraft (platform and antennas) is given in presently unpublished data by G. D. Qualls et al. of the Langley Research Center. Reflector and strongback structure development and structural dynamic issues associated with the large-diameter reflector and long feed mast of the LFMR are presented in reference 2.

HFMS Antenna

The high-frequency microwave sounder provides data on tropospheric temperature, humidity, precipitation and ice-size profiles, precipitation coverage and rates, and cloud water estimates. These measurements are obtained using frequencies of 60, 90, 118, 160, 183, and 220 GHz. This instrument is an offset-fed Cassegrain antenna, as illustrated in figure 2, consisting of an electronic feed, a parabolic primary reflector, a subreflector, and the associated electronic data gathering, processing, and distribution equipment. The main structural components are the primary reflector with its supporting strongback and the feed support mast.

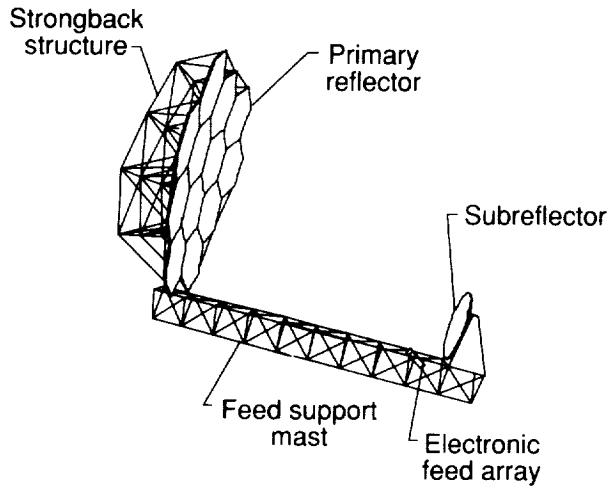

Figure 2. 7.5-m-diameter high-frequency microwave sounder antenna.

Primary reflector. The HFMS primary reflector provides an optimal spatial resolution of approximately 8 km at 220 GHz from geosynchronous orbit. Figure 3 illustrates the relationship between spatial resolution (Earth footprint), altitude, operating frequency, and antenna diameter. At the lower frequencies, the resolution worsens, stretching to approximately 29 km at 60 GHz. If higher resolution is needed at the lower frequencies, the antenna diameter must be increased or the antenna must be placed in a lower-altitude orbit. Resolutions provided by a 7.5-m-diameter antenna are representative of current scientific goals (ref. 1).

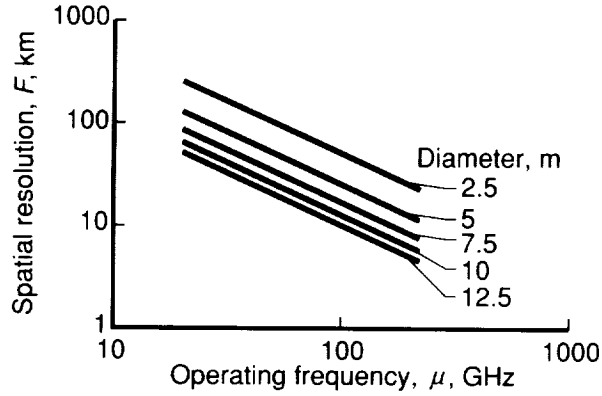

Figure 3. Spatial resolution as function of altitude (H), antenna diameter (D), and operating frequency (μ). H = 35 760 km; $F = 1.2(H/D)(C/\mu)$ where C denotes the speed of light (in meters per second).

In addition to a large diameter, a reflector used for geosynchronous microwave radiometry must have a highly accurate surface. Estimates of the antenna surface accuracy needed for microwave radiometry, measured in terms of root-mean-square (rms) surface error, range from $\lambda/50$ (ref. 3) to $\lambda/100$ (ref. 4), where λ is the wavelength of the associated operating frequency. For the HFMS concept, the smallest value of λ is 0.136 cm (220 GHz). Using these estimates as guidelines suggests a maximum allowable rms surface error between 13.6 μm (0.53 mil) and 27.0 μm (1.06 mils).

This accuracy requirement dictates the use of a solid surface. However, the size of the reflector (a 7.5-m diameter) cannot be accommodated by any currently available launch vehicle (4.4 m maximum for the Shuttle orbiter). This suggests the need for some form of segmented reflector that can be deployed or assembled in orbit. The reflector concept in this analysis consists of a set of polished reflector surface panels individually supported at the joints of a tetrahedral truss strongback that can be assembled in orbit. The reflector panels are composed of a graphite or glass composite honeycomb structure with a high-reflectivity surface that minimizes the thermal distortions across individual panels.

The concept of a tetrahedral truss strongback is derived from an experimental test-bed model (ref. 5) under study in the Precision Segmented Reflector (PSR) program. The goal of this program is to develop and test the strongback structure, reflector,

and other related technologies for application to submillimeter wavelength (optical) applications. The shape of the reflector for this antenna is an offset parabola with a ratio of focal length to diameter (f/D) of 1.5 necessary for high-quality measurement and scanning capabilities.

An aluminized surface coating is assumed to cover the front face of the reflector to provide the required high radio frequency (rf) reflectivity and to minimize the temperature excursions and resulting distortions of the panels. The backside of the antenna (the side facing the strongback structure) is covered with multilayer insulation (mli) to further control heat transfer to and from the panels.

Strongback structure. The main function of the tetrahedral truss strongback is to provide a stable support structure that minimizes distortions in the overall shape of the reflector. The truss must precisely maintain the relative positions and orientations of the individual panels with respect to the feed and the other panels.

The baseline structure of the tetrahedral truss strongback (fig. 4) is composed of thin-tube elements of uncoated P75 graphite/epoxy composite, aluminum joints, and end fittings. The tetrahedral truss was selected for its advanced level of development, design heritage, and its lightweight, high-strength characteristics. Assumed thermophysical properties of the truss elements are given in table 1.

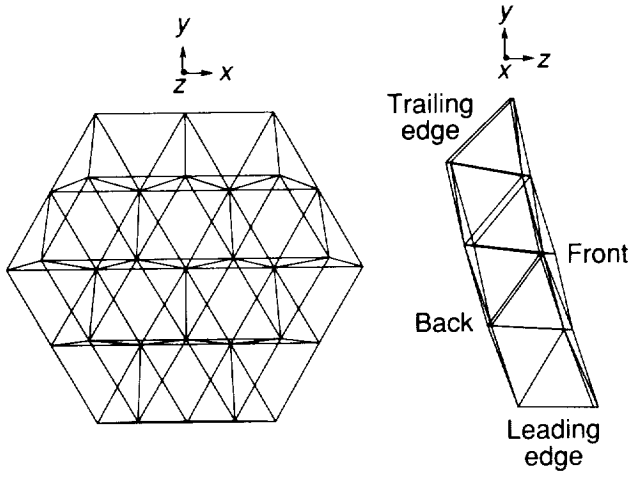

Figure 4. Baseline structure of tetrahedral truss strongback.

Since each structural element consists of both tubes and end fittings, estimation of the element CTE must consider the CTE's of both tubes and end fittings. The equation for the element CTE is based on the CTE's of both components and on the length fraction of the end fittings to the entire length of the element. Thus,

$$(\mathrm{CTE})_{\mathrm{eff}} = (\mathrm{CTE})_t + \mathrm{LF}\left[(\mathrm{CTE})_j - (\mathrm{CTE})_t\right]$$

where $(\mathrm{CTE})_{\mathrm{eff}}$ denotes the effective element CTE, $(\mathrm{CTE})_t$ denotes the CTE of the tube, $(\mathrm{CTE})_j$ denotes the CTE of the end fittings, and LF denotes the length fraction (the total length of both end fittings divided by the entire length of the element). The PSR test-bed element (ref. 5) is fabricated of unidirectional tubes of P75 graphite/epoxy composite (CTE $= -1.08 \times 10^{-6}$ cm/cm-°C), each with two aluminum end fittings (CTE $= 23.4 \times 10^{-6}$ cm/cm-°C) that are 13 cm in length (32.3 percent of the entire length of the element). The resulting element CTE was calculated to be 6.7×10^{-6} cm/cm-°C. For the baseline concept of this analysis, the length of the end fittings remained consistent with that in reference 5, but the length of the graphite tubes increased such that the length fraction became 12.2 percent, thus giving an element CTE of 1.9×10^{-6} cm/cm-°C.

Table 1. Assumed Strongback Thermophysical Properties

	Front	Back	Diagonals
Element structural sizes:			
Diameter, cm	2.5	2.5	2.5
Thickness, mm	3.0	3.0	3.0
Average length, m	2.15	2.15	2.06
Material (P75 graphite/thermoplastic):			
Young's modulus, N/m^2	2.07×10^{11}		
Mass density, kg/m^3	1740		
Specific heat, J/kg-°C	850		
Thermal conductivity, W/m-°C	76		
Element coefficient of thermal expansion (CTE), cm/cm-K	1.9×10^{-6}		
Surface thermal properties:			
Solar absorptivity (α)	0.9 (uncoated)		
Thermal emissivity (ε)	0.8 (uncoated)		

The baseline surface properties are those of uncoated graphite. The ratio of solar absorptivity to thermal emissivity (α/ε) of this reference case is close to unity; alternative coatings with α/ε ratios less than and greater than unity are also considered in the analysis.

The material properties and structural integrity of some candidate graphite composites may vary or degrade at elevated temperatures (above 100°C), but the thermoplastic composites used in the original

PSR concept are cured at higher temperatures and thus can withstand temperatures higher than the 100°C level. However, the 100°C level is used as a guideline for comparison. The properties listed above are assumed not to vary with temperature.

Feed system. A scanning multiple-beam feed system provides global coverage using a single primary reflector. The system is based on the offset-fed Cassegrain multiple-reflector concept (ref. 6) and consists of an electronic feed array, a secondary reflector (subreflector), and the necessary feed support mast, as shown in figure 2. In the HFMS concept, the incoming microwave signal reflects first off the primary reflector and then off the secondary reflector into the feed array. The subreflector and feed array may scan slightly, thus enlarging the coverage area provided by the antenna. The focal length f of the primary antenna is 11.25 m, based on $f/D = 1.5$. By using the "folded" optics of the Cassegrain system, a 1-m subreflector placed approximately 10 m from the reflector provides the necessary separation, and slightly reduces the length of the supporting feed mast.

The feed mast selected for the HFMS is based on the "Minimast" concept (ref. 7). The Minimast is a deployable, retractable, multiple-bay, repeating triangular truss structure made of graphite/epoxy composite tubes and aluminum-alloy hinges and end nodes. The Minimast was developed as a ground test article to better characterize the performance and control of large space structures and thus is used in this model as a starting point for future design efforts because of its known structural performance. Structural characteristics of the feed-mast-equivalent beam structural model are given in table 2.

Table 2. Structural Characteristics of Feed Beam

Type	Minimast (triangular truss)
Material	Graphite/epoxy
Axial stiffness, N	1.15×10^8
Bending stiffness, N-m^2	1.22×10^7
Torsional stiffness, N-m^2	1.10×10^6
Mass per unit length, kg/m	4.8

Antenna mass summary. The tetrahedral truss strongback is constructed of 102 tube elements and 31 lumped mass elements representing the joints and end fittings. Using the element sizes and masses of table 1, the strongback mass is 131 kg. The reflector panels have an areal density of 10 kg/m^2, including a provision for surface control actuators. This results in a total primary reflector mass of 440 kg. The 1-m-diameter subreflector mass is 13 kg, assuming the same areal density as the primary reflector. The Minimast feed structural characteristics (table 2) result in a beam mass of 54 kg. The feed array mass of 72 kg is an estimate from reference 8. The overall mass of the HFMS is 710 kg.

Thermal and Structural Analyses

Thermal and structural analyses were performed on the HFMS antenna strongback using integrated computer-aided engineering software packages developed for the design and analysis of large space systems. The software packages are described in the appendix.

Thermal Analysis

Thermal analyses were performed to determine element temperature variations for the uncoated graphite truss under different orbit conditions. In addition, the effectiveness of alternative element surface coatings as well as a Sun shield was examined as a means of reducing temperature excursions and improving surface accuracy. The analyses included formulation of thermal models based on the finite-element model, selection and quantification of orbit heating conditions, and calculation of truss element temperatures for the baseline and alternative thermal control concepts.

Thermal model. The thermal model used for determining internal heat transfer in this analysis consists of the truss supporting structure and the solid reflector surface. The feed, feed mast, and subreflector are not included. Each truss element is assumed to be isothermal and is connected to other elements through joints modeled as lumped masses. The reflector is modeled using triangular thin-shelled elements (which approximate the thermal characteristics of a honeycomb panel). The reflector is included in the analysis to assess its impact on the thermal behavior of the truss. The modes of heat transfer in the model are conductive and radiative coupling with the primary mode being radiative. Most of the internal heat transfer in the model occurs between the reflector and the individual truss elements (via radiation); the heat transfer between truss elements (whether by conduction or radiation) is quite small.

Heating and cooling of truss elements in this analysis was strongly influenced by the presence of the reflector. View factors between the truss elements and the reflector elements (the percentage of heat leaving one surface that is incident on another) were on the order of 0.1. More importantly, the low solar absorptivity (thus high solar reflectivity) of the

mli results in large amounts of reflected solar energy impinging on the truss elements and elevating their temperatures during already hot conditions. During a portion of the orbit, the reflector shadows the truss elements, thus preventing any type of heating and allowing their temperatures to drop to severely low levels. This shadowing effect occurs every orbit and is relatively independent of both the season and the Sun's declination. Shadowing by the truss elements is also included in the analysis but has a much less significant impact.

Conductive coupling between the elements is based on the axial thermal conductivity of the truss and joint materials, the length of the elements, and the cross-sectional area of the elements where they intersect the joint. For the long, thin, low-conductivity tubes of this structure, only small conductive coupling exists between truss elements. This is further reduced by imperfect thermal connections between the joint and tube. No conduction is assumed between the reflector panels and the truss by virtue of the extremely low conductance actuators connecting them.

The radiative coupling between elements depends primarily on the view factors of the elements and their surface properties (solar absorptivity and, primarily, thermal emissivity). The view factors between the truss elements were calculated to be on the order of 0.001 or smaller, thus resulting in low radiative coupling. When thermal coatings are applied to the elements, the resulting heat transfer becomes negligible when compared with that between the reflector panels and the truss elements.

Thermal environment. The thermal environment experienced by the HFMS in geosynchronous orbit is defined by the external radiative heat fluxes from the Sun and Earth, the space heat sink, the existence and length of eclipse periods, and the internal heat exchanges. External heat sources incorporated in the analysis include direct and reflected incident solar radiation, solar radiation reflected from Earth (solar albedo), and incident Earth radiation (Earth thermal). Solar albedo and Earth thermal radiation depend on distance from the Earth and are insignificant (less than 1 percent of the total heating) at geosynchronous altitude when compared with incident solar heating. Truss cooling is induced by cold space, which is assumed to be a black body at 4 K, and by eclipses that occur each orbit during equinox seasons. The slow rotation of the reflector and strongback relative to the Sun (characteristic of a geosynchronous Earth-oriented body) results in a long exposure to both heating and cooling conditions and, consequently, in severe temperature extremes.

In order to bracket the thermal environment extremes, the thermal analysis considered two different orbits: one occurring during equinox (which includes a 72-min eclipse) and one occurring during solstice (no eclipse), as shown in figure 5.

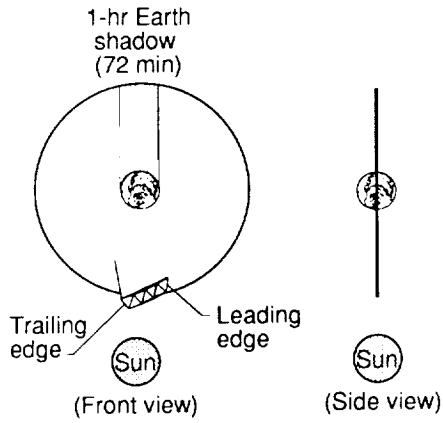

(a) Equinox.

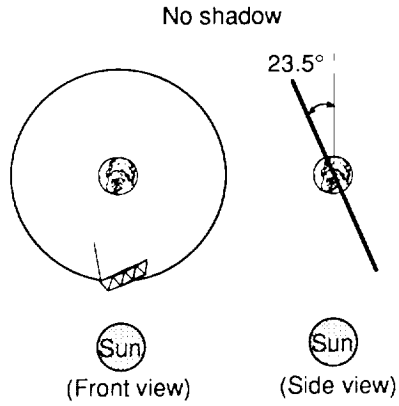

(b) Solstice.

Figure 5. Description of equinox and solstice orbits.

External heating rates. External heating rates (primarily direct solar radiation) are calculated on the strongback elements at 12 different positions around the orbit. For the equinox orbit, additional heating rates are calculated just before and after entering and exiting the Earth's shadow. Figure 6 shows the orbital variation of external heating rates averaged over all the uncoated truss elements for both the equinox and solstice orbits beginning at 0°, or local noon (where the antenna is directly between the Sun and the Earth).

Heating rates are primarily influenced by three factors: the change in element orientation relative to the Sun, the solar radiation reflected from the back of the reflector, and the blockage caused by the reflector.

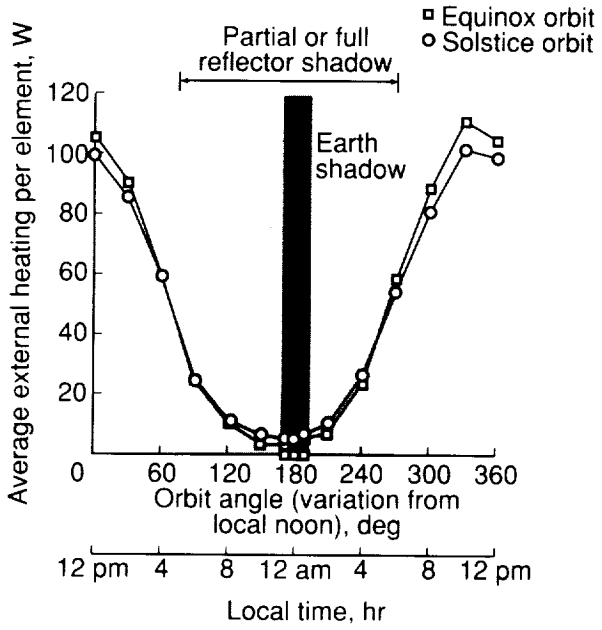

Figure 6. Variation of average external heat input with orbit position.

As the strongback progresses through its orbit, the orientation of the elements relative to the Sun can vary from parallel, producing minimal heating, to perpendicular, producing maximum heating. In complex lattice-type structures such as the tetrahedral truss concept, a wide assortment of element orientations exists and changes with time. The distribution of these orientations causes severe local temperature gradients and distortions that have an impact on the antenna performance.

In addition to direct illumination by the Sun, the truss elements also receive a large amount of solar radiation from reflection off the back of the reflector during Sun periods. The solar radiation striking some elements is almost doubled when the back of the reflector is pointing directly at the Sun. The offset nature of the antenna concept (fig. 2) causes this doubling to occur at an orbit position slightly removed from solar noon. As the back of the reflector points away from the Sun, the reflected solar energy and resulting rate of heating decrease substantially, as shown in figure 6 for both orbit cases. In the solstice case, shown in figure 5, a tilt angle exists between the orbit plane and the Sun vector. This tilt (which reduces the energy striking the reflector and, consequently, the reflected energy and heat by the sine of the tilt angle) results in lower average heat fluxes than in the equinox case during Sun periods.

Reflector blockage begins at an orbit angle of approximately 75° and noticeably reduces heating on the elements. This reduced heating is similar in magnitude for both orbit cases and occurs during every orbit. The slight tilt of the solstice case keeps more of the elements from being shadowed by the reflector than in the equinox case. The solstice cases retain slightly higher average heating values. Figure 6 illustrates these higher average heating values that occur between the orbit angles of 120° and 250°, as most of the elements move behind the reflector.

The effect of the Earth's shadow can be seen on the equinox heating curve as the small but sharp drop occurring around 180°, local midnight.

Although the heating and cooling are similar for both orbits, the slightly more extreme heating and cooling of the equinox orbit and the presence of the Earth's shadow produce a more diverse thermal environment, thereby leading to greater thermal distortions. Consequently, the equinox orbit was selected as the worst-case orbit, and all results presented here are based on this case unless otherwise specified.

Temperature characteristics of baseline concept. Temperatures were computed for each element in each orbital position and are used in the distortion analysis. Average temperatures for all elements were also examined through the various orbits and are useful for showing trends and understanding the complex heating/cooling of Earth-orbiting spacecraft. Figures 7 and 8 show minimum, maximum, and average temperature variations for the baseline truss elements at 1-hr (15°) intervals beginning at local noon (0°) in the equinox orbit for steady-state (equilibrium) and transient conditions.

Wide temperature variations are experienced by the truss elements, ranging from 115°C to 250°C for the steady state and from 115°C to 160°C for the transient analysis. The temperature difference between the maximum and minimum element temperatures at a given orbit position also varies significantly, up to a maximum of 190°C. As the average and minimum temperatures drop, the maximum temperature remains relatively constant. (This maximum is the hottest temperature in the truss, which does not necessarily occur on the same element at each position.) The effect of the Earth's shadow can be seen by the sharp drop and ensuing rise in maximum element temperatures occurring around 180° (local midnight). However, the sharp drop is less for the minimum and average steady-state temperatures

and is quite small for any of the transient temperatures. The average drops more gradually as more of the elements move into the shadow of the reflector at orbit positions ranging from around 75° to 180°. As the elements move out of the reflector shadow (about 180°), the element average temperature rises less quickly than the maximum.

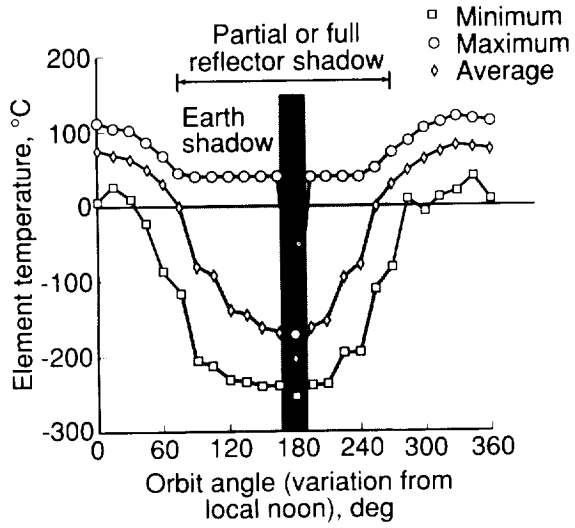

Figure 7. Variation of equilibrium (steady-state) element temperature with orbit position for uncoated truss elements in equinox orbit.

The steady-state temperatures can be helpful for understanding more about the environment at any given orbit position by representing equivalent sink temperatures. However, these results can provide misleading information about the temperatures that the elements actually experience, and where the worst conditions exist. For instance, according to the steady-state results, the maximum temperature difference across the truss is 290°C and occurs at orbit positions of 165° and 195°, whereas the transient results indicate that a maximum temperature difference of 190°C occurs at 240°. Since surface distortions are proportional to temperature difference, the 290°C difference would lead to excessively large distortion estimates.

Figure 9 shows the transient temperature variation for the uncoated elements versus orbit position for the solstice orbit. A significant drop is observed in the minimum, maximum, and average element temperatures as the elements move behind the reflector, similar to figure 8. All three solstice curves are similar in shape and magnitude to the equinox curves except that there is no Earth shadow period for the solstice orbit case during which the maximum temperatures drop and rise sharply. Upon closer examination, a slight increase in average temperature is seen for the solstice orbit during the reflector shadow periods and a slight decrease during the Sun periods. This trend is due to the fact that the antenna is tilted 23.5° relative to the Sun for the solstice case. This tilt reduces the sunlight reflected off the backside of the reflector onto the truss, which in turn reduces the average temperature of some of the truss elements from 115°C to 109°C at the hottest orbit position. The tilt also prevents more of the truss elements from being shadowed by the reflector, thus keeping their temperatures relatively high and increasing the average temperature from 160°C to 150°C at the coldest orbit position.

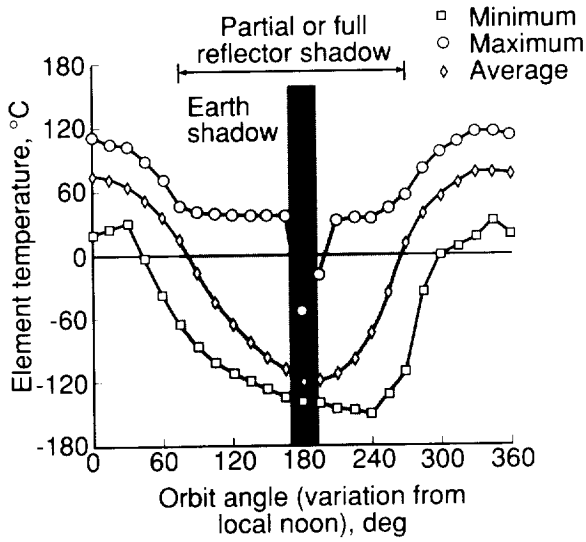

Figure 8. Variation of transient element temperature with orbit position for uncoated truss elements in equinox orbit.

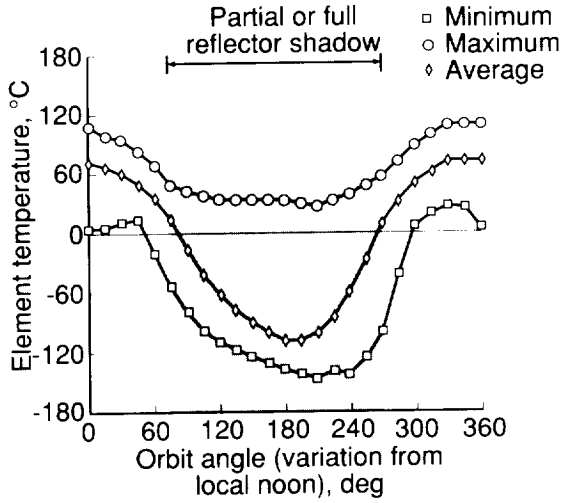

Figure 9. Variation of transient element temperature with orbit position for uncoated truss elements in solstice orbit.

Alternative thermal protection techniques. High temperatures not only cause distortion of the truss and degrade antenna performance but also may deteriorate the structural materials. For example, at temperatures above 100°C, some graphite composites may begin to decompose, thus leading to catastrophic failure in the strongback. As shown in figure 8, maximum temperatures during Sun periods are calculated to exceed this value. Consequently, some form of thermal protection is needed to prevent these high temperatures and possibly reduce surface distortions. Two methods of protecting the truss structure are (1) to directly coat each structural element with a thin surface coating and/or (2) to enclose the entire strongback truss structure within a Sun shield.

Coating. An etched aluminum coating fabricated directly on the graphite tubes has surface properties, i.e., absorptivity (α) and emissivity (ε), that can be adjusted during fabrication by controlling the etching process. Two different α/ε ratio coatings were considered in this analysis: a low-ratio (0.3/0.65) coating and a high-ratio (0.3/0.2) coating.

Minimum, maximum, and average temperatures are presented in figures 10 and 11 for each of the two surface coatings for the equinox orbit. In figure 10 (the low α/ε ratio case), a desirable decline in all element temperatures occurred at orbit positions around 0°, or local noon. This decline is attributed to the favorable heat balance set up by the low α/ε ratio. The lower absorptivity reduces the amount of heat absorbed by the elements, and the higher emissivity allows more of the heat absorbed from the Sun to be rejected to space, thus reducing all temperatures. The reduced temperature variation across the truss at each orbit angle, measured as the difference between the maximum and minimum temperatures, will help minimize surface distortions.

The high α/ε ratio coating concept also reduces the temperature variation across the truss, but its lower emissivity restricts heat rejection and results in temperatures well above the 100°C level during Sun periods (fig. 11). During the shadow period, this restricted heat rejection allows the temperatures to remain hotter which helps to minimize the surface distortions.

The results of the coated-element analysis indicate that both of the coatings produce desirable results but have associated problems. Based on these results, the ideal surface would have a low α/ε ratio (less than 1.0) for sunlight operation and a low emissivity (approximately 0.2) for night or shadow operation. However, coatings with these properties that will meet the long-mission times and be easily producible are not readily available.

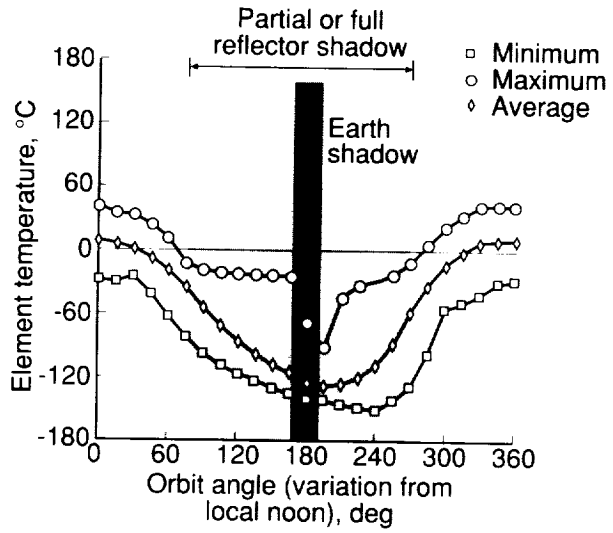

Figure 10. Variation of transient element temperature with orbit position for low-ratio (α/ε = 0.3/0.65) coated elements in equinox orbit.

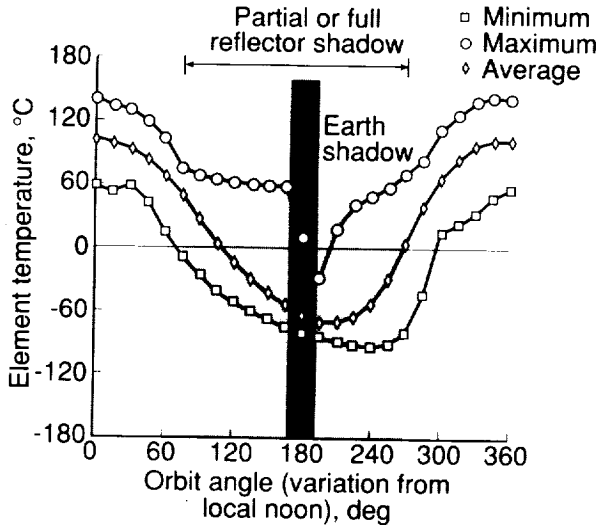

Figure 11. Variation of transient element temperature with orbit position for high-ratio (α/ε = 0.3/0.2) coated elements in equinox orbit.

Sun shield. The alternative to these coatings is the Sun shield which prevents exposure of the uncoated elements to both the Sun and cold space, thus reducing heat gain and loss by the truss elements. Enclosing the strongback structure in a semirigid Sun shield is an attempt to completely insulate the entire structure from the environment. The shield in this analysis was assumed to be 1-mm-thick aluminized Kapton with α/ε ratios of 0.35/0.6 on the outside

and 0.3/0.2 on the inside. The drawback of the Sun shield, however, is that it contributes additional mass and assembly concerns to the system. Since the Sun does not directly impinge on the elements, the maximum temperatures are reduced. Also, temperatures occurring during shadowing remain higher since the elements are viewing the warmer Sun shield rather than cold space. This concept prevents degradation of the structural integrity of the material by maintaining temperatures well below the material limits (fig. 12). It also reduces possible distortions by preventing element temperatures from radically falling or rising during shadowed periods and by maintaining small temperature gradients across the truss.

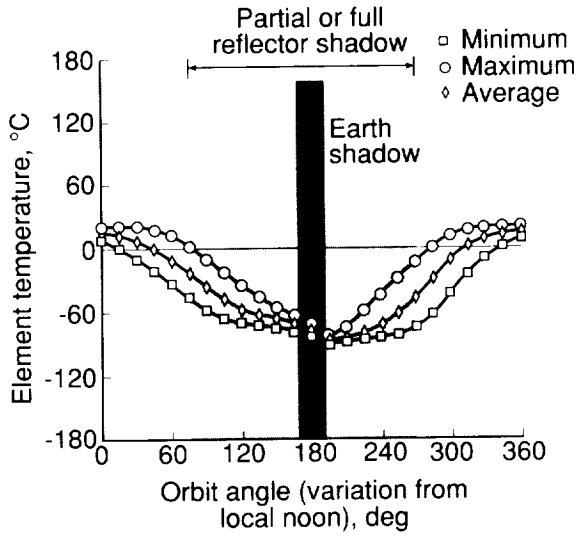

Figure 12. Variation of transient element temperature with orbit position for truss elements enclosed in Sun shield in equinox orbit.

Comparisons. Figures 13 and 14 provide a comparison of average element temperatures and the standard deviation in element temperatures across the truss, respectively, at each orbit position for the four alternatives. The average temperature curves from figures 8, 10, 11, and 12 are combined in figure 13 to better compare the effects of the thermal designs. For instance, the low-ratio coating reduces the temperatures during sunlit periods, whereas the low-emissivity coating reduces heat loss during shadowed periods. Additionally, the two coated concepts tend to have reduced temperature variations compared with those of the uncoated concept (fig. 13). The Sun shield has an even flatter temperature curve because the shield prevents direct exposure to the Sun or shadow, thus limiting both the high and low temperatures. The shield concept, however, has shadow-period temperatures slightly lower than the high-ratio-coating concept. Although the elements cool down less for the Sun-shield concept, their temperatures before cooling down are already significantly lower. Thus, the coldest temperatures of the Sun shield are noticeably less than those of the high-ratio concept.

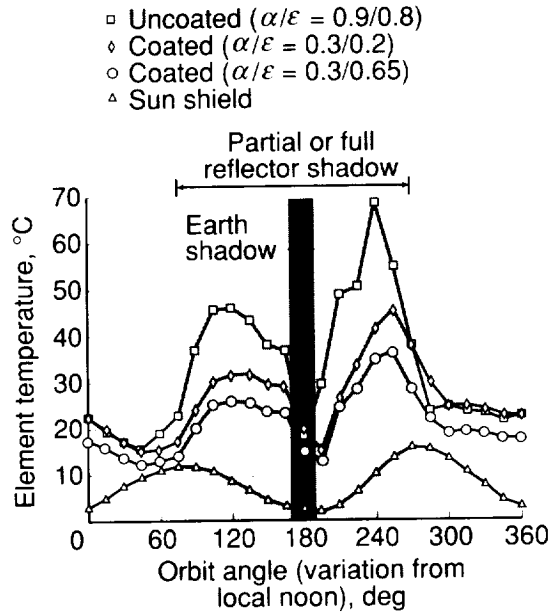

Figure 13. Variation of standard deviation in element temperature across strongback with orbit position in equinox orbit.

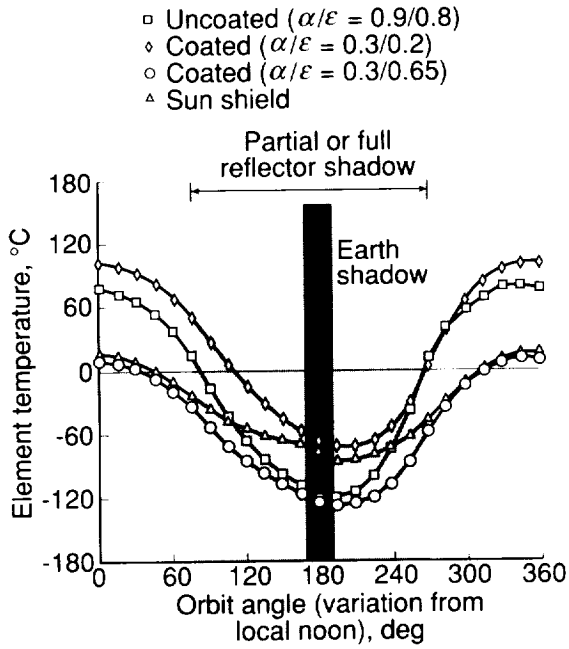

Figure 14. Variation of average element temperature with orbit position in equinox orbit.

The standard deviation in temperatures as a function of orbit position (fig. 14) is a better estimate of

the actual overall temperature variation across the truss. The standard deviation as a function of orbit position for the alternatives is similar in that it can be characterized by two peaks. For the uncoated and coated cases, one peak occurs just as the reflector starts to shadow the elements, and the other peak occurs as they become unshadowed. The two peaks for the Sun-shield concept occur as the antenna presents the minimum projected area toward the Sun. The magnitude of deviation of the alternative concepts varies significantly with the uncoated elements having the highest deviation, followed by the high-ratio coating, the low-ratio coating, and finally the Sun-shield concept whose highest deviation is an almost negligible 12°C (fig. 14).

Structural Analysis

As the antenna moves throughout its orbit, the elements expand or contract depending on the thermal expansion properties and the change in temperature relative to the temperature of the undeformed structure (assumed to be 22°C or room temperature for this analysis). The distortion of a given element is also dependent on the distortions of the nearby elements and thus on their temperatures. A linear static structural analysis was performed to calculate the thermal distortions and stresses of the reflector support structure and to estimate their effect on antenna performance.

The baseline finite-element structural model was used with the addition of a restraint condition. Three central nodes on the backside of the truss were restrained, preventing both translation and rotation. Although this restraint condition may not represent a worst case, it mathematically restrained the problem and represented a possible means of attachment to the platform. A linear static analysis was performed at each orbit position by inputting the corresponding individual element temperatures into the model, and the resulting node displacements and element stresses experienced by the truss strongback at each orbit position were obtained.

For the worst case examined (the uncoated concept), typical element stresses are on the order of 3.5×10^7 N/m^2, which pose no problems.

As an example of how the truss distorts, figure 15 illustrates displacements experienced by the front side of the strongback at an equinox orbit position of 210° for the baseline concept. The distorted configuration of the front side of the truss shown superimposed on the undistorted configuration demonstrates the shrinkage and added curvature that result from the extreme cold. Distortions are amplified graphically for better visualization. Node-displacement magnitudes as large as 0.78 mm were calculated for this configuration. These displacements are better understood when evaluated in terms of the overall shape changes of the antenna surface.

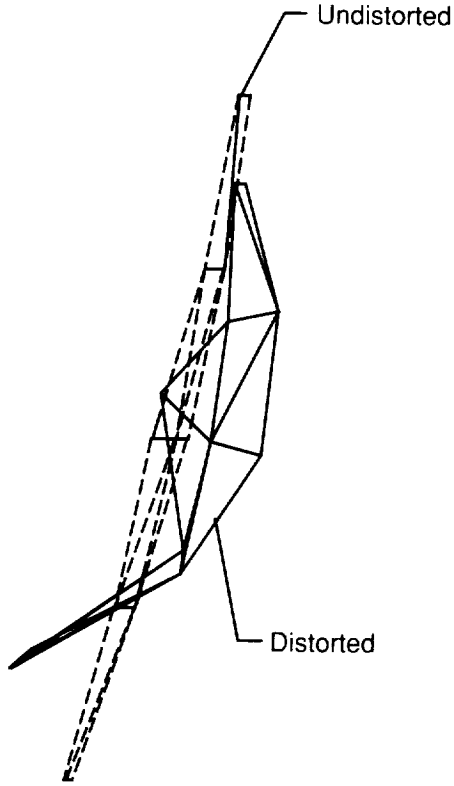

Figure 15. Front side of thermally distorted strongback for uncoated concept at orbit angle of 210°.

Best-fit-parabola analysis. Shape changes are quantified using the Utku-Schmele best-fit-parabola technique (ref. 9) which calculates the characteristics of a new parabola that most closely fits through the distorted node locations on the front side of the strongback supporting the reflector as calculated from the linear static analysis. These characteristics are shown in figure 16. The defocus or change in focal length describes the curling up or flattening out of the reflector support nodes. The pointing error describes the rotation of the best-fit-parabola focal direction from the undistorted focal direction. Suggested accuracy limits (ref. 10) for complete antenna defocus and pointing error are twice the wavelength (±2.73 mm) and 10 percent of the beamwidth (±4.31 arcsec at 220 GHz), respectively. These limits are presented herein for comparative purposes only since they represent complete system error, whereas the calculated results do not include the effects of the feed-beam distortion. Once the best-fit parabola is determined, this technique calculates the root-mean

square (rms) error between the actual distorted node locations and the corresponding locations on the new parabola. This error (also shown in fig. 16) is an estimate of the surface roughness caused by the thermal distortions and can be used to determine the beam efficiency of the antenna.

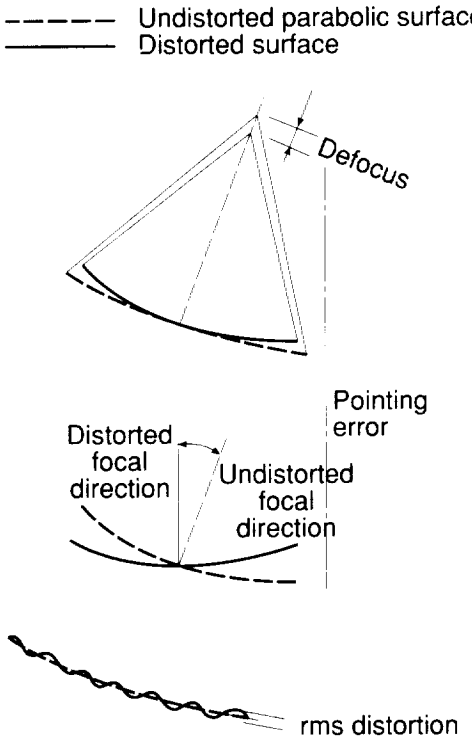

Figure 16. Best-fit-parabola performance characteristics.

Distortion characteristics. Figures 17, 18, and 19 show the defocus, pointing error, and rms surface error results, respectively, for all four alternative concepts in the equinox orbit. Contour plots of surface distortion at four orbit positions are shown in figure 20.

Baseline (uncoated) concept. At local noon, the baseline concept is fully in the Sun with extra heat reflecting from the back of the reflector surface onto the elements, thus causing temperatures to be quite high. Most of the elements in the truss are at temperatures higher than the undeformed temperature. These elevated temperatures cause the elements to elongate, expanding the truss. The front side of the truss tends to flatten (fig. 20(a)). Positive displacements (along the z-axis) over most of the reflector surface and negative displacements along the edges are observed. This flattening increases the focal length of the reflector, as indicated by the positive defocus in figure 17. Also, because the reflector is attached to the feed mast at the trailing edge, the mean upward displacement of the strongback causes the reflector to point more toward the feed mast as indicated by the negative pointing error in figure 18. The deviation in temperature at this location is relatively small, as seen in figure 13, and there are no particularly hot or cold regions (no large temperature gradients) and no sharp displacement gradients (fig. 20(a)). Consequently, the rms error (fig. 19) is relatively low.

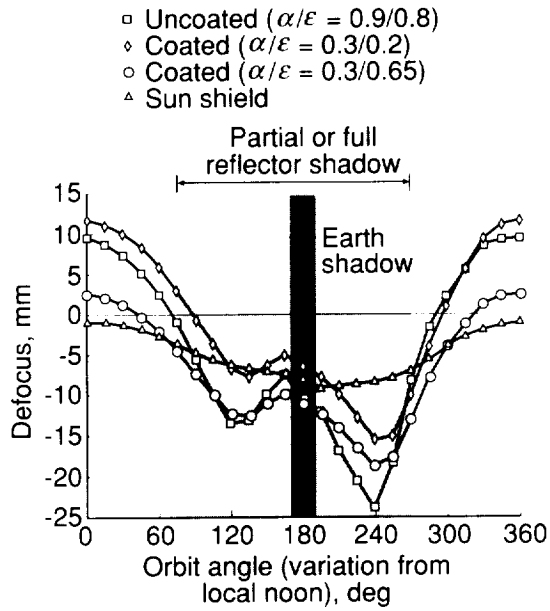

Figure 17. Variation of reflector defocus with orbit position for four alternative thermal designs.

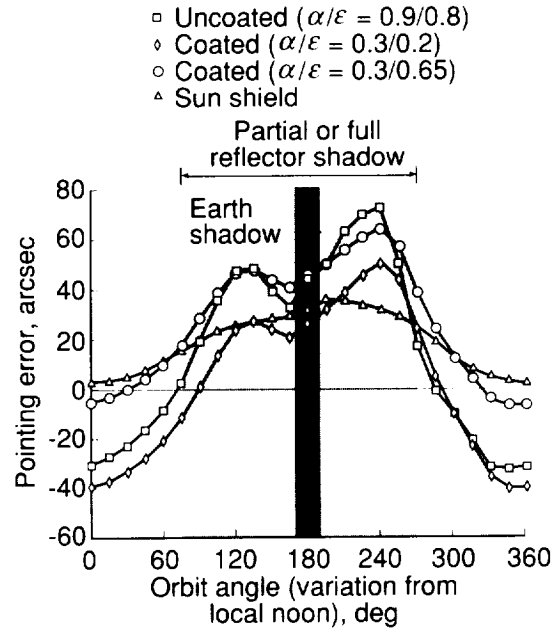

Figure 18. Variation of reflector pointing error with orbit position for four alternative thermal designs.

As the antenna revolves around the Earth, its orientation changes relative to the Sun, thus reducing the reflected energy that strikes the elements. Element temperatures drop, the elongation in elements reduces, and the truss begins to curl toward its undeformed dimensions, as indicated by reduced magnitudes in defocus and pointing error (at orbit positions between 0° and 60°). However, some of the diagonal elements are still at elevated temperatures, causing slight displacements of the front surface nodes (indicated by the slight rms error in fig. 19).

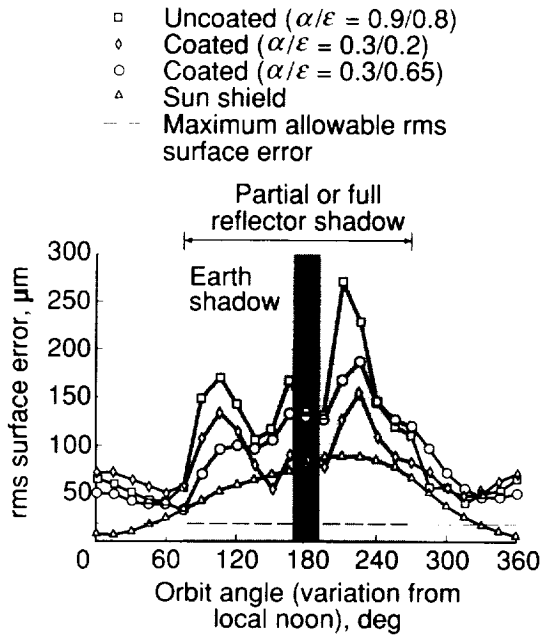

Figure 19. Variation of reflector rms surface error with orbit position for four alternative thermal designs.

The antenna reflector is slightly offset from the z-axis (fig. 4) such that regions of the truss enter the reflector shadow at an orbit position of about 75°. The elements shadowed initially include most of the front-side truss elements, the backside truss elements on the leading edge, and the diagonals on the leading edge. The temperatures of these elements drop significantly and become lower than the reference temperature. Consequently, these elements begin to shrink and the front side of the truss curls, causing a decrease in the focal length and an increase in the magnitude of defocus. Since the rest of the backside elements are not shadowed and are no longer impinged upon by reflected sunlight, they cool slightly which contributes to overall shrinkage. Some of the diagonals in the trailing region and right and left edges of the strongback are, however, more exposed now to the direct sunlight and are still quite warm. These elements elongate and cause substantial localized displacement of the front side nodes on the trailing side, thus increasing the curvature and causing the reflector to point slightly away from the feed mast. More significantly, large displacement gradients (fig. 20(b)) occur in the right and left edges of the strongback, which cause relatively high rms surface errors, as illustrated in figure 19 by the first peak occurring at an orbit position of 105°.

As the reflector rotates further, more of the diagonals are shadowed and reoriented, the large localized displacements reduce in size and number, and the rms surface error is reduced. The defocus and pointing error remain relatively high, however, because of the shrinkage caused by the decreasing temperatures of most of the elements. As the elements in the trailing region cool further, their temperatures approach the temperatures of the remainder of the truss. The temperature deviation is reduced, and the defocus and the pointing error decrease.

Just before the entire truss is shadowed by the reflector at 165°, certain front-side elements on the trailing edge become almost normal to the incident solar radiation. Their temperatures become quite high compared with those of the rest of the truss as seen in figure 8. Those elements elongate and the resulting localized displacements and large gradients (fig. 20(c)) again increase the rms error, as illustrated by the second peak in figure 19. The defocus and pointing error, however, continue to decrease slightly because of the reduced temperature deviation (fig. 13) in the trailing regions of the truss.

As the antenna enters the Earth's shadow (180°), temperature deviations fall as every element is shadowed from the Sun, but this extra cooling causes additional shrinkage and results in an increased defocus and pointing error despite the falling temperature deviations. Also, the rms error is smaller, a result of the reduced temperature gradients.

Between orbit positions of 195° and 210°, some of the leading-edge truss elements (more specifically, the leading diagonals and bottom elements) exit the shadow and heat up almost instantly, because of their low thermal mass. The affected diagonals elongate; this further increases the curvature (and, consequently, the defocus and pointing error) and produces large localized displacements (fig. 20(d)) and the largest rms surface errors.

As more of the diagonals exit the shadow, the localized displacements become smaller, reducing the rms error. However, as the leading-edge element temperatures continue to rise, elongating the leading edge of the surface, the defocus and pointing error continue to rise along with the temperature standard deviation.

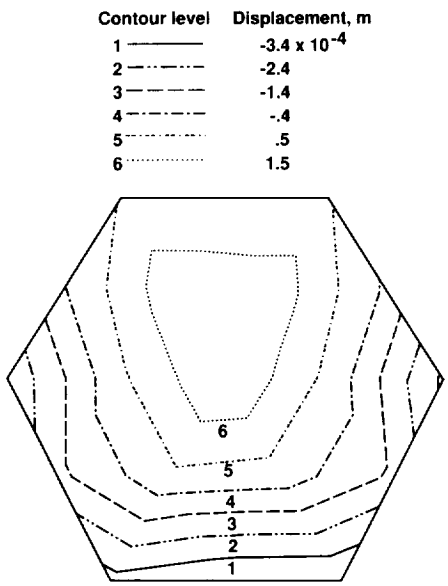

(a) Orbit position of 0° (local noon).

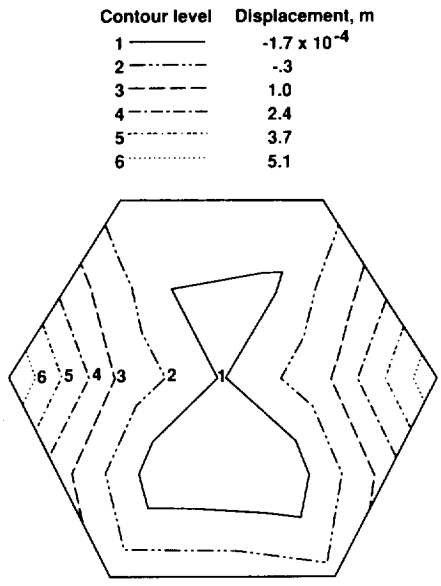

(b) Orbit position of 105°.

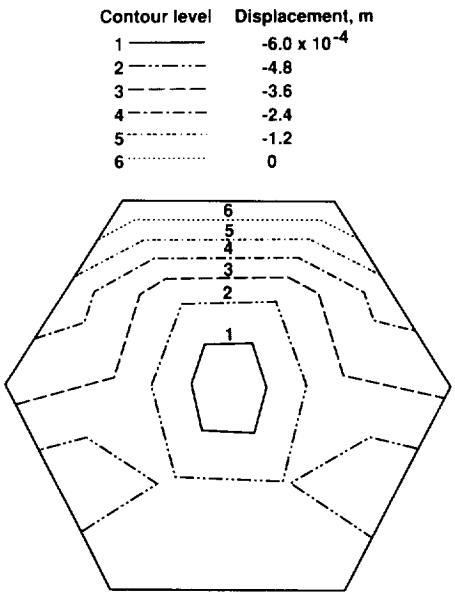

(c) Orbit position of 165°.

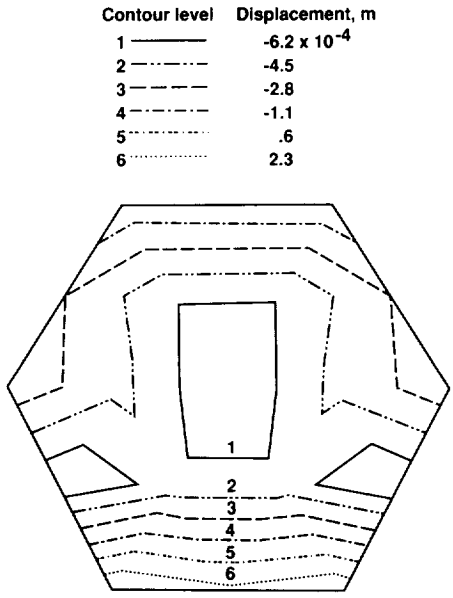

(d) Orbit position of 210°.

Figure 20. Surface contours of displacements along z-axis at four orbit positions.

Finally, as the front side of the truss exits the shadow (around 270°), the temperature deviation across the truss diminishes and the average temperature approaches the undeformed temperature. The defocus, pointing error, and rms surface error decrease. Heating continues until the undeformed temperature is exceeded and the truss flattens, again increasing the defocus and pointing error.

Alternative concepts. When the elements are coated or protected by the Sun shield, the temperature variations across the truss are decreased. The effect of this temperature reduction on the surface-distortion results is different for each concept. For example, during the warmest parts of the orbit (around local noon), the elements covered with the low-ratio coating do not experience a large temperature

increase and therefore do not elongate significantly. Consequently, the defocus and pointing error are also small relative to those of the uncoated elements. On the other hand, the elements with the high-ratio coating (and therefore higher temperatures) tend to elongate more than the uncoated elements, and this results in larger defocus and pointing errors.

As the truss begins to enter the shadow, the low-ratio coating prevents the diagonals (which caused local displacements for the uncoated concept) from heating up as quickly or as much. This, in addition to the already lower temperatures, results in smaller temperature gradients and smaller rms surface errors relative to the uncoated and high-ratio-coating concepts. The high-ratio coating also diminishes the gradients but not to the same degree.

During the shadowed portions of the orbit, the defocus and pointing error for the two coated concepts do not oscillate as much as those for the uncoated concept. The coated concepts maintain the smaller defocus and pointing errors by virtue of warmer element temperatures, although the low-ratio-coating concept has the colder temperatures and, consequently, worse defocus and pointing errors. The local gradients and rms surface errors are still smaller for the coated concepts during this period, although the low-ratio-coating concept has worse rms surface errors than those of the high-ratio concept. This is, again, attributed to the colder temperatures of this concept.

As the truss starts to exit the shadow and the leading-edge elements begin to warm, the already relatively warm temperatures of the high-ratio coating limit the large gradients and the resulting rms surface error. The low-ratio coating also reduces the rms surface error (compared with the uncoated truss) by decreasing the temperature rise of the leading-edge elements. However, this smaller temperature rise and the extremely cold shadow temperatures still result in rms surface errors larger than the high-ratio concept.

Based on these results, neither coating is significantly better than the other in all cases, and in some cases each is even worse than the uncoated baseline concept. Both coating concepts have wide temperature variations throughout the orbit and a large temperature deviation across the truss which lead to excessive surface distortions, although they are usually less than those at the baseline.

The Sun shield decreases both the orbital variation in temperature as well as the deviation across the truss and, as shown in figures 17, 18, and 19, causes reduced surface distortions throughout almost the entire orbit. The variation in surface distortion appears to be driven primarily by the average temperature of the elements rather than by the gradients or the deviation. The Sun shield reduces the gradients and deviations by preventing localized visibility of any heat source by the elements and by promoting heat exchange between the elements by reflecting energy from one onto the others, instead of allowing the energy to escape to space.

Alternative structural materials. When comparing the performance of these alternatives to the surface accuracy requirements, it can be seen that even the Sun-shield concept, with its greatly reduced surface error, does not meet the 13.6-μm requirement, nor does it meet the defocus or pointing error requirements. One technique that may be necessary to meet this requirement is to actively control the surface with actuators attached to the joints of each reflector panel. The application of this technology is under development as a part of the PSR program and is beyond the scope of this paper.

Another approach is to employ elements with lower effective CTE's. Effective CTE values for elements depend upon a number of factors including the type of material used for the tubes and end fittings, the geometry of the material (e.g., the lay-up of the composites), and the overall geometric characteristics of the components comprising the element (e.g., the relative lengths of the tube and end fitting). The baseline structural concept, composed of tubes of unidirectional P75 graphite/epoxy composite and two aluminum end fittings with a length fraction of 12.2 percent, had an element CTE of 1.9×10^{-6} cm/cm-°C. By reducing the length fraction or selecting a different material for the end fittings, the element CTE can be reduced substantially.

Figure 21 demonstrates the effects on element CTE due to reduction in the end-fitting length fraction and selection of alternative end-fitting materials. These curves were generated using the equation for element CTE presented earlier. As can be seen, element CTE can be driven quite low by using smaller length fraction end fittings. However, certain constraints (manufacturing tolerances, astronaut and ground handling, and tube interface requirements) on the length of end fittings limit the extent to which they may be shrunk. A more effective means is to select alternative materials like steel (CTE = 1.31×10^{-5} cm/cm-°C) or titanium (CTE = 8.28×10^{-6} cm/cm-°C) that are more prevalent in actual space-structure applications. Using the same

length fraction, element CTE's of 0.66×10^{-6} and 0.062×10^{-6} cm/cm-°C can be obtained for the steel, and titanium selections, respectively (fig. 21).

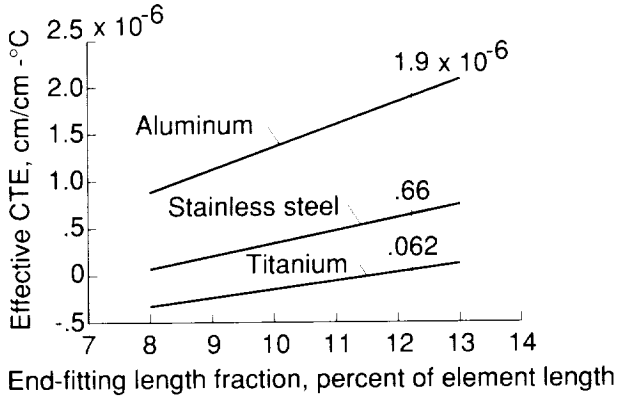

Figure 21. Variation of effective element CTE with end-fitting length fraction for three alternative end-fitting materials.

Figure 22 shows the orbital variation in rms surface error for both the uncoated and the Sun-shield configurations for three element CTE values (1.9×10^{-6}, 0.66×10^{-6}, and 0.062×10^{-6} cm/cm-°C) for aluminum, stainless steel, and titanium end fittings, respectively. In calculating these distortions, no new temperature profiles were calculated. It was assumed that small changes in the thermal conductivity and thermal capacitance of the end fittings would not noticeably change the temperatures calculated for the elements. Since the conductivities and thermal capacitances of the three materials are similar, this assumption should be valid. Commensurate with a linear static analysis, a linear relationship exists between element CTE and rms distortion such that each reduction in CTE resulted in a similar multiplicative reduction in rms surface error (and in defocus and pointing error). However, although the reduction in surface error for steel end fittings is significant, the surface error still exceeds requirements throughout most of the orbit, even for the Sun-shield configuration. With titanium end fittings, on the other hand, even the most severe surface errors on the uncoated configuration fall within the requirements over the entire orbit. The same holds true for reflector defocus and pointing error. The Sun-shield and coated configurations with titanium end fittings can provide adequate surface accuracy for even slightly higher frequencies. However, should significantly higher accuracy requirements or frequencies be called for, an active control system may be more applicable.

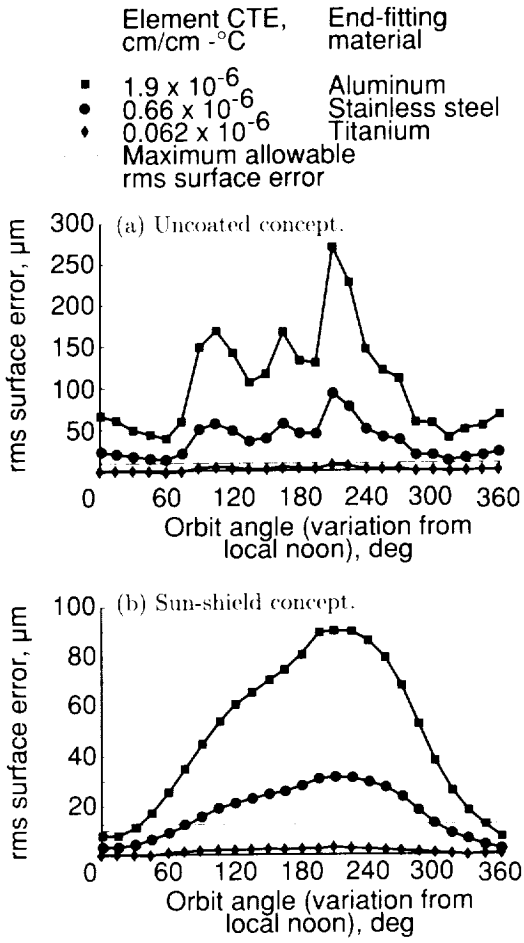

Figure 22. Variation of rms surface error with element CTE and orbit position for two thermal designs.

Concluding Remarks

A thermal-structural model has been created and analyses have been conducted on the tetrahedral truss strongback concept for a 7.5-m-diameter microwave radiometer antenna. Orbital variations in temperature were calculated and discussed. Performance comparisons were made between four thermal-protection alternatives. Finally, thermal distortions were discussed for these alternatives in regard to three antenna performance parameters: defocus, pointing error, and root-mean-square surface error.

Temperatures were shown to range from 150°C to 180°C depending on orbit position and surface coating. The temperatures were strongly influenced by shadowing, particularly the shadow cast by the reflector surface. The effects of this shadow were felt throughout a large portion of both the equinox and solstice orbits. The shadow cast by the reflector was much more prominent than that cast by the Earth with the result that both orbits were similar with minor differences due to the presence of the Earth's shadow. Mixed success was

achieved by the use of coatings in alleviating the various thermal problems. Although the coating with the lower absorptivity/emissivity ratio maintained temperatures within suggested material limits throughout the orbit, it allowed excessive temperature drops and thermal distortions during the shadowed portions of the orbit. The coating with the high absorptivity/emissivity ratio reduced these distortions but allowed maximum temperatures to approach suggested material limits during the sunlit periods. The Sun shield performed the best, both in maintaining moderate temperatures and in reducing distortions. However, these reduced distortions still exceeded the surface accuracy required for this mission.

The surface accuracy, pointing, and defocus requirements can be satisfied for frequencies at or below 220 GHz by proper selection of element materials to provide an effective element coefficient of thermal expansion near or below 1.0×10^{-7} cm/cm-°C coupled with application of truss element surface coatings, preferably with a low thermal emissivity and a low absorptivity/emissivity ratio (less than 1). Should thermoplastics be used, permitting higher element temperatures, a higher ratio coating can be more functional. Use of a Sun (or thermal) shield would extend this limit to slightly higher frequencies. However, for significantly higher frequencies or stricter requirements, some form of active surface control may be required. Although these results were for this particular design, the trend in temperature and thermal distortion should apply to any similarly sized antenna having a solid reflector and tetrahedral truss strongback that is planned for geosynchronous operation.

NASA Langley Research Center
Hampton, VA 23665-5225
July 19, 1990

Appendix

Modeling and Analysis Tools

The structural and thermal analyses were performed using the system of computer-aided engineering software shown in figure A1. This software includes the Tetrahedral Truss Structural Synthesizer (TTSS) (for easy finite-element model development), Supertab (for visual inspection and modification of finite-element models and postprocessing of results), Thermal Model Generator (TMG) (for thermal modeling and analysis), Model Solution (for linear, static structural analysis), and Antperf. A brief discussion of these tools follows.

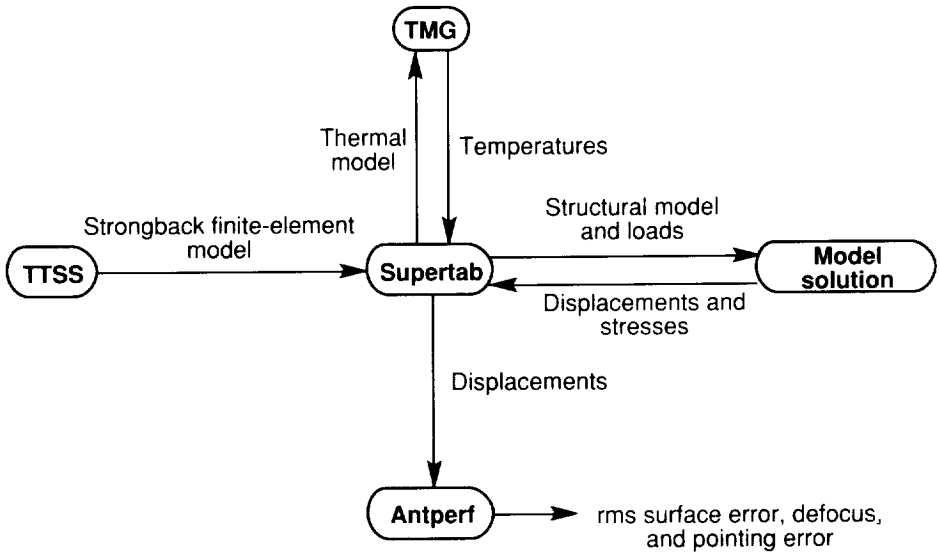

Figure A1. Thermal structural analysis tools and data flow.

Tetrahedral Truss Structural Synthesizer

TTSS was created by General Dynamics Corporation to quickly model repetitive tetrahedral truss structures to be used to support large antenna reflectors and platforms. TTSS was originally part of the Large Advanced Space Systems program (ref. 11).

TTSS, which is interactive in nature, requests limited information from the user about the overall antenna characteristics such as antenna diameter, f/D ratio, and number of truss bays. More detailed information such as structural-element physical and material properties, design loads, and hinge and joint characteristics can also be supplied by the user. This information is used to estimate the structural-element sizes, overall mass properties, and number of piece parts that make up the structure and to create a finite-element model of the structure to be used by various analysis programs.

Supertab

Supertab is part of the I-DEAS software system developed by the Structural Dynamics Research Corporation (SDRC) and described in reference 12. It is used to interactively build, visualize, and modify finite-element models prior to structural analysis and to visually interrogate the results of such an analysis. The reflector structural models created by TTSS are automatically translated to Supertab where other components are modeled and added to complete the entire antenna structural model. These models are analyzed in TMG or Model Solution discussed below; the results (such as temperatures, deflections, and stresses) are automatically translated back to Supertab for postprocessing.

Thermal Model Generator

TMG is an integrated thermal analysis tool developed by MAYA Heat Transfer Technologies Ltd. of Canada that works in conjunction with SDRC's Supertab to perform complete thermal modeling and analysis tasks (ref. 13). More specifically, TMG accepts the finite-element geometric model output from Supertab and employs an interactive menu-driven input system to build a complete lumped-parameter (or finite-difference) thermal model that can be used to estimate steady-state or transient element temperatures for subsequent thermal-structural analysis.

In building this thermal model, TMG performs several intermediate functions: it translates finite-element model data into a surface model for calculation of radiation heat transfer characteristics

and into a finite-difference thermal network model by calculating conductive couplings and thermal capacitances; it calculates radiation exchange view factors, radiative couplings and orbital heat fluxes (including the effects of shadows and reflections) using techniques based on diffuse enclosure assumptions; it uses these radiative couplings and heat fluxes along with the translated finite-difference model to calculate steady or transient temperature distributions and heat transfer rates employing thermal network techniques and various matrix solution algorithms; it maps these temperatures back onto the finite-element model and translates them into Supertab for graphical postprocessing and as input to Model Solution. TMG performs these functions in an integrated nature, thus automating the entire process.

Model Solution

Model Solution is the primary numerical solver for the I-DEAS software package (ref. 14). Its direct connection with Supertab significantly automates modeling, analysis, and visualization of results. Its linear-static structural analysis capability, used for this study, is based on a finite-element formulation of linearized structural deformation equations. Inputs include the finite-element model built in Supertab, the restraint set or boundary conditions discussed earlier, and the element temperatures that act to produce structural loads. Model Solution estimates the displacements of the nodes in the finite-element model of the reflector strongback as well as element stresses caused by these loads and translates them back to Supertab where they can be graphically examined. These displacement results are also translated into a form suitable by Antperf.

Antperf

Antperf is a program based on a surface accuracy routine discussed in references 9 and 11 that performs a best-fit-parabola analysis on the distorted strongback to calculate its overall distortion characteristics such as pointing error, defocus, and rms surface error. Antperf uses finite-element data from Supertab and displacement data from Model Solution to calculate the best-fit parabola through the displaced nodes of the strongback which would support the reflector surface and determine the change in focal length and orientation of this new parabola from the original undistorted parabola. It then compares the distorted node locations with the node locations of the new (best-fit) parabola to determine the rms distortion of the reflector.

References

1. Pidgeon, David Joseph: *A Subsystem Design Study of an Earth Sciences Geostationary Platform.* M.S. Thesis, George Washington Univ., 1989.
2. Wahls, Deborah M.; Farmer, Jeffery T.; and Sleight, David W.: *On-Orbit Structural Dynamic Performance of a 15-Meter Microwave Radiometer Antenna.* NASA TP-3041, 1990.
3. Lovelace, U. M.; and Garrett, L. B.: Large Space Systems Requirements, Deployable Concepts, and Technology Issues. *Aerospace Century XXI: Space Flight Technologies. Vol. 64, Part II, Advances in the Astronautical Sciences*, George W. Morgenthaler, and W. Kent Tobiska, eds., Univelt, Inc., 1987, pp. 1019 1034. (Available as AAS 86-394.)
4. Hedgepeth, John M.: *Structures for Remotely Deployable Precision Antennas Final Report.* NASA CR-182065, 1989.
5. Collins, Timothy J.; and Fichter, W. B.: *Support Trusses for Large Precision Segmented Reflectors: Preliminary Design and Analysis.* NASA TM-101560, 1989.
6. Hannan, Peter W.: Microwave Antennas Derived From the Cassegrain Telescope. *IRE Transactions on Antennas and Propagation*, vol. AP-9, no. 2, Mar. 1961, pp. 140 153.
7. Adams, Louis R.: *Design, Development and Fabrication of a Deployable/Retractable Truss Beam Model for Large Space Structures Application.* NASA CR-178287, 1987.
8. Foldes, Peter: *A Design Study for the Use of a Multiple Aperture Deployable Antenna for Soil Moisture Remote Sensing Satellite Applications.* NASA CR-178154, 1986.
9. Ludwig, A., ed.: *Computer Programs for Antenna Feed System Design and Analysis. Volume I: Programs and Sample Cases.* NASA CR-84810, 1967.
10. Dyer, J. E.: *Development of a Verification Program for Deployable Truss Advanced Technology.* NASA CR-181703, 1988.
11. Leondis, Alex: *Large Advanced Space Systems Computer-Aided Design and Analysis Program Final Technical Report.* NASA CR-159191-1, 1980.
12. *Supertab Engineering Analysis Pre- and Post-Processing User Guide.* I-DEAS Level 4, Structural Dynamics Research Corp., 1988.
13. *TMG Thermal Model Generator A Thermal Analysis Computer Program (TMG User's Manual).* Revision 2.2, MAYA Heat Transfer Technologies Ltd., Montreal, Canada, 1988.
14. *Supertab Engineering Analysis Model Solution and Optimization User Guide.* I-DEAS Level 4, Structural Dynamics Research Corp., 1988.

NASA
National Aeronautics and Space Administration

Report Documentation Page

1. Report No.	2. Government Accession No.	3. Recipient's Catalog No.
NASA TP-3016		

4. Title and Subtitle	5. Report Date
Thermal-Distortion Analysis of an Antenna Strongback for Geostationary High-Frequency Microwave Applications	September 1990
	6. Performing Organization Code
7. Author(s)	8. Performing Organization Report No.
Jeffery T. Farmer, Deborah M. Wahls, and Robert L. Wright	L-16739
9. Performing Organization Name and Address	10. Work Unit No.
NASA Langley Research Center Hampton, VA 23665-5225	506-49-21-02
	11. Contract or Grant No.
12. Sponsoring Agency Name and Address	13. Type of Report and Period Covered
National Aeronautics and Space Administration Washington, DC 20546-0001	Technical Paper
	14. Sponsoring Agency Code

15. Supplementary Notes

16. Abstract

The Global Change Technology Initiative calls for a geostationary platform for Earth-science monitoring. One of the major science instruments is the high-frequency microwave sounder (HFMS) which uses a large-diameter, high-resolution, high-frequency microwave antenna. The size and required accuracy of this antenna dictate the need for a segmented reflector, and on-orbit disturbances may be a significant factor in its design. A study was performed to examine the effects of the geosynchronous thermal environment on the performance of the strongback structure for a proposed antenna concept for this application. The study included definition of the strongback and a corresponding numerical model to be used in the thermal and structural analyses, definition of the thermal environment, determination of structural element temperatures throughout potential orbits, estimation of resulting thermal distortions, and assessment of the capability of the structure to meet surface accuracy requirements. Analyses show that shadows produced by the antenna reflector surface play a major role in increasing thermal distortions. Through customization of surface coatings and element expansion characteristics, the segmented reflector concept can meet the strict surface accuracy requirements.

17. Key Words (Suggested by Authors(s))

Geostationary microwave radiometer
Large space structures
Thermal analysis and control
Antenna structural performance
Structural analysis
Computer-aided engineering and analysis

18. Distribution Statement

Unclassified—Unlimited

Subject Category 18

19. Security Classif. (of this report)	20. Security Classif. (of this page)	21. No. of Pages	22. Price
Unclassified	Unclassified	20	A03

For sale by the National Technical Information Service, Springfield, Virginia 22161-2171

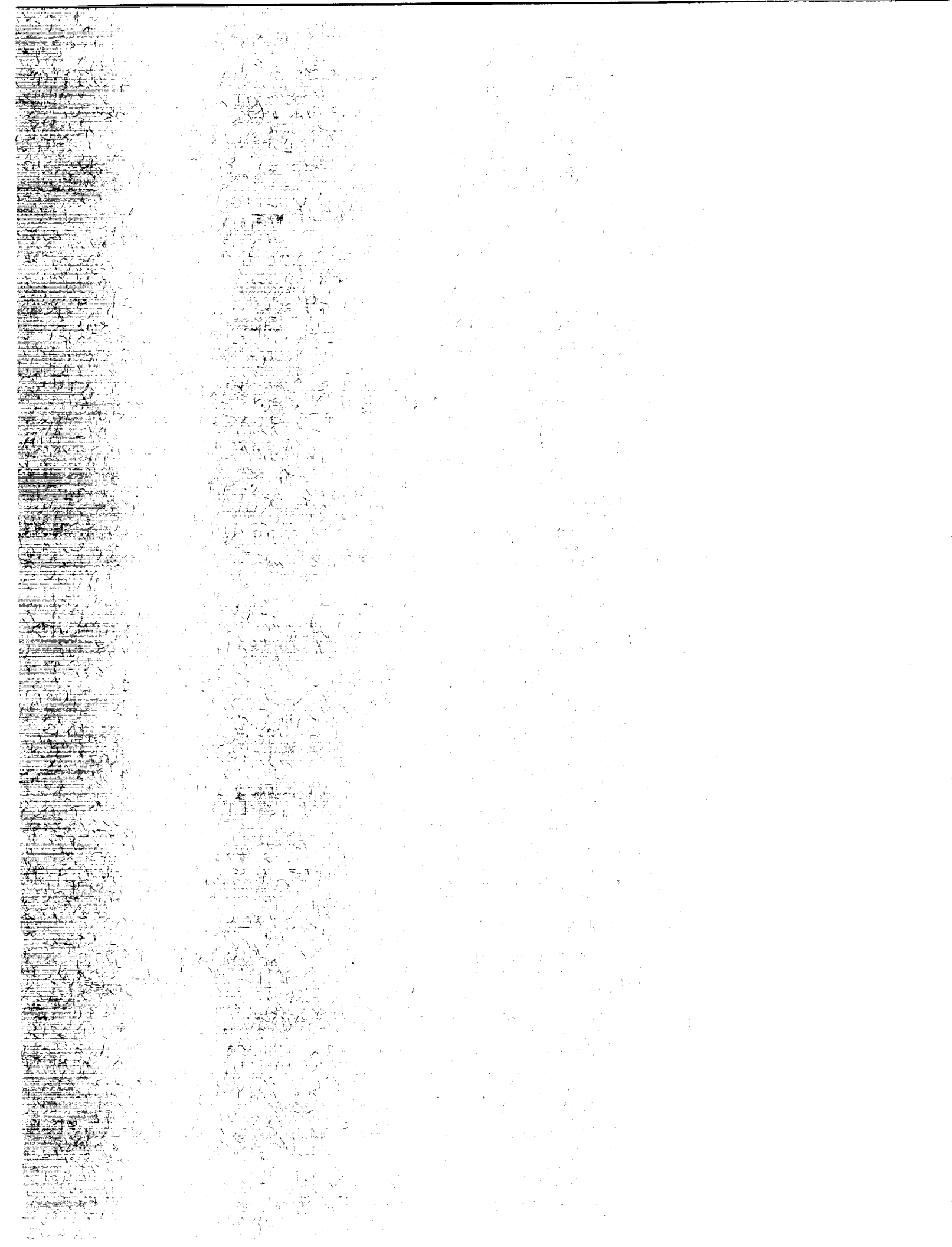

National Aeronautics and
Space Administration
Code NTT-4

Washington, D.C.
20546-0001

Official Business
Penalty for Private Use, $300

BULK RATE
POSTAGE & FEES PAID
NASA
Permit No. G-27

NASA

POSTMASTER: If Undeliverable (Section 158
Postal Manual) Do Not Return